Journal Pre-proof

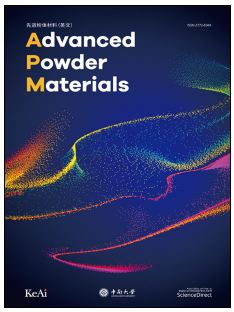

Cobalt Phosphosulfide Nanoparticles Encapsulated into Heteroatom-Doped Carbon as Bifunctional Electrocatalyst for Zn-Air Battery

Xiaolong Xu, Shuo Wang, Shiquan Guo, Kwan San Hui, Jiameng Ma, Duc Anh Dinh, Kwun Nam Hui, Hao Wang, Lipeng Zhang, Guowei Zhou

PII: S2772-834X(21)00027-0

DOI: https://doi.org/10.1016/j.apmate.2021.12.003

Reference: APMATE 27

To appear in: *Advanced Powder Materials*

Received Date: 19 December 2021

Accepted Date: 20 December 2021

Please cite this article as: X. Xu, S. Wang, S. Guo, K. San Hui, J. Ma, D.A. Dinh, K.N. Hui, H. Wang, L. Zhang, G. Zhou, Cobalt Phosphosulfide Nanoparticles Encapsulated into Heteroatom-Doped Carbon as Bifunctional Electrocatalyst for Zn-Air Battery, *Advanced Powder Materials*, https://doi.org/10.1016/j.apmate.2021.12.003.

Graphical abstract

Cobalt Phosphosulfide Nanoparticles Encapsulated into Heteroatom-Doped Carbon as Bifunctional Electrocatalyst for Zn-Air Battery

Cobalt phosphosulfide (CoPS) nanoparticles encapsulated with S, P, N tri-doped carbon (SPNC) is proposed as bifunctional electrocatalyst of oxygen reduction reaction (ORR) and oxygen evolution reaction (OER) derived from zeolitic imidazolate framework-67. A flexible Zn–air battery with CoPS@SPNC delivers a low overpotential of 0.49 V, a high energy efficiency above 80%, and a stable discharge voltage of 1.29 V at 2 mA cm^{-2} for 80 h.

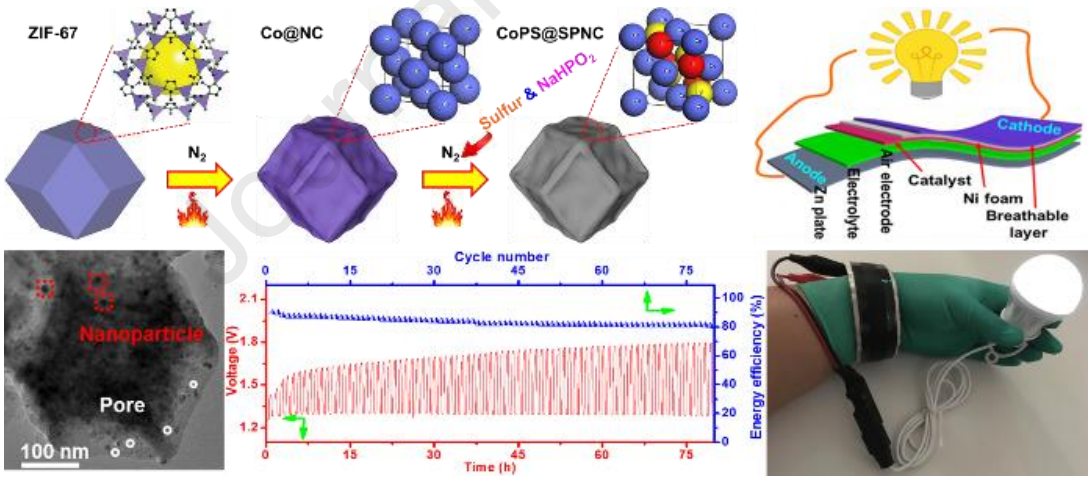

Cobalt Phosphosulfide Nanoparticles Encapsulated into Heteroatom-Doped Carbon as Bifunctional Electrocatalyst for Zn-Air Battery

Xiaolong Xu [abcd†], Shuo Wang[d†], Shiquan Guo [b], Kwan San Hui [*,c], Jiameng Ma [f], Duc Anh Dinh [e], Kwun Nam Hui [*,d], Hao Wang [*,b], Lipeng Zhang [*,f], Guowei Zhou [*,g]

[a] School of Materials Science and Engineering, Qilu University of Technology (Shandong Academy of Sciences), No. 3501, Daxue Road, Changqing District, Jinan, Shandong Province, People's Republic of China.

[b] The College of Materials Science and Engineering, Beijing University of Technology, Beijing, People's Republic of China.

[c] Engineering, Faculty of Science, University of East Anglia, Norwich, United Kingdom.

[d] Joint Key Laboratory of the Ministry of Education, Institute of Applied Physics and Materials Engineering, University of Macau, Avenida da Universidade, Taipa, Macau SAR, China.

[e] NTT hi-tech Insitute, Nguyen Tat Thanh University, Ho Chi Minh city 700000, Vietnam.

[f] College of Energy, State Key Laboratory of Organic Inorganic Composites, Beijing University of Chemical Technology, Beijing 100029, China.

[g] Key Laboratory of Fine Chemicals in Universities of Shandong, Jinan Engineering Laboratory for Multi-scale Functional Materials, School of Chemistry and Chemical Engineering, Qilu University of Technology (Shandong Academy of Sciences), Jinan 250353, P. R. China.

[†] These authors contributed equally

[*] Corresponding authors

1 Kwan San Hui (k.hui@uea.ac.kr)

2 Kwun Nam Hui (bizhui@um.edu.mo)

3 Hao Wang (haowang@bjut.edu.cn)

4 Lipeng Zhang (zhanglp@buct.edu.cn)

5 Guowei Zhou (gwzhou@qlu.edu.cn)

Acknowledgements: This work was supported by the funding from Qilu University of Technology (Shandong Academy of Sciences), the Science and Technology Development Fund, Macau SAR (File no. 191/2017/A3, 041/2019/A1, 046/2019/AFJ), the National Natural Science Foundation of China (Grant Nos. 51972180), the Multi-Year Research Grants (MYRG2017-00216-FST and MYRG2018-00192-IAPME) from the Research Services and Knowledge Transfer Office at the University of Macau, and UEA funding.

Cobalt Phosphosulfide Nanoparticles Encapsulated into Heteroatom-Doped Carbon as Bifunctional Electrocatalyst for Zn-Air Battery

Abstract: The design of non□noble electrocatalysts with low overpotential, high effectiveness, and good cycling stability for oxygen evolution reaction (OER) and oxygen reduction reaction (ORR) is highly desirable for high-performance Zn–air batteries. Herein, CoPS nanoparticles encapsulated with S, P, N tri-doped carbon material (SPNC) is proposed as bifunctional electrocatalyst of ORR and OER derived from zeolitic imidazolate framework-67. Density functional theory calculations consistently reveal that P element in CoPS@SPNC improve the electrical conductivity and reduce OH* hydrogenation energy barrier on Co sites, thereby facilitating the overall ORR/OER activities. A flexible Zn–air battery with CoPS@SPNC delivers an overpotential of 0.49 V, an energy efficiency above 80%, and a discharge voltage of 1.29 V at 2 mA cm^{-2} for 80 h. Such strategy could provide numerous possibilities for the design of highly efficient electrocatalysts.

Keywords: Bifunctional electrocatalyst; Zeolitic imidazolate framework; Heteroatom doping; Zn–air battery

1. Introduction

Intermittent and nonconstant renewable energy requires exploitation of highly efficient energy storage and conversion technologies [1-3]. Electrochemically rechargeable Zn–air batteries (ZABs) are promising candidates in energy storage systems because of their safety, eco-friendliness, and high specific energy density (1084 Wh kg^{1}) [4-7]. However, the high cost, poor stability, and scarcity of noble Pt□, Ir□, and Ru□based electrocatalysts have been the bottlenecks for the large-scale implementations of ZABs [8, 9]. Accordingly, developing nonprecious metal electrocatalysts with high reaction kinetics is highly imperative to the anticipated renewable energy technologies [10-12].

Recently, considerable efforts have been invested in developing non-noble metal bifunctional electrocatalysts for oxygen evolution reaction (OER) and oxygen reduction reaction (ORR) [13-15]. Among various nonprecious catalysts, nanostructured cobalt sulfides (CoS, CoS_2, and Co_9S_8) have been investigated as bifunctional oxygen electrocatalysts for ZABs because of their low cost and environmental compatibility. However, cobalt sulfides have low reaction kinetics and unsatisfactory electrical conductivity [16-18], which lead to limited catalytic activity. These limitations can be overcome by integrating cobalt sulfides with highly conductive carbonaceous materials. In particular, zeolitic imidazolate framework (ZIF)-derived hybrids can fully expose active catalytic sites and facilitate mass transport due to high porosity and large surface area, which is conducive to favorable catalytic performance. Heteroatom doping is an effective strategy used to tune the

reaction free energy and electronic structure for enhancing the catalytic properties of the electrocatalysts. For instance, incorporation of N and P atoms into CoS_2 significantly increased the electrical conductivity and enhanced the OER and ORR activity of CoS_2, achieving a reduced gap of charge and discharge (0.8 V at 10 mA cm^{-2}) in ZAB [17]. The enhanced electrocatalytic performance of P-doped CoS_2 is attributed to modulating the electronic structure of CoS_2 due to high electron-donating ability of P. Furthermore, heteroatoms (such as N, S, and P) doped in carbon has gained considerable attention because dopants can effectively polarize the adjacent carbon atoms and modify the electronic structure, offering more active sites and decreasing the reaction adsorption free energy of O_2 for high ORR and OER activity [19-21]. For instance, Gao et al. [22] reported that N, P codoped hollow carbon could be a good bifunctional ORR/OER catalyst, which displayed a low potential deviation of 0.73 V between the half-wave potential for ORR and the potential reaching 10 mA cm^{-2} for OER. Therefore, developing ZIF-derived metal sulfides/carbon hybrid possessing favorable kinetics toward ORR/OER for ZAB through simultaneous heteroatom doping on cobalt sulfides and carbon is highly desirable yet challenging.

Here, we reported CoPS nanoparticles (NPs) embedded into P, S, N tri-doped carbon (SPNC) through carbonization of ZIF-67 followed by a sequential and simultaneous sulfidation and phosphidation. The CoPS@SPNC electrocatalyst exhibits large surface area and tuned porosity feature that are beneficial to mass transportation and reaction kinetics. Moreover, P element can effectively regulate the electrical structure and charge distribution, reducing the reaction free energy of the rate□limiting

step toward ORR and OER. As an electrocatalyst, CoPS@SPNC exhibited high ORR and OER kinetics in alkaline solution, as well as delivers an overpotential of 0.49 V, energy efficiency higher than 80%, and a discharge voltage of 1.29 V at 2 mA cm^{-2} for 80 h in flexible ZABs.

2. Experiment

2.1. Catalyst preparation

The synthesis of ZIF-67 was described in supporting information. For Co@NCs, as-prepared ZIF-67 were placed in a tube furnace and maintained at 500 °C, 600 °C, and 700 °C for 1 h with a heating rate of 2 °C min^{-1} under flowing N_2 atmosphere, labeling as Co@NC-500, Co@NC-600, and Co@NC-700, respectively. For CoPS@SPNC, Co@NC-600 powders, sulfur powder, and $NaHPO_2$ powder were placed a tube furnace and maintained at 300 °C for 1 h in with a heating rate of 2 °C min^{-1} under flowing N_2 atmosphere. The as-prepared CoPS@SPNC sample was collected after cooling to room temperature without any treatment for further use.

2.2. Characterization

The structures, compositions, and morphologies of the samples were analyzed using X-ray diffraction (XRD), scanning electron microscope (SEM), transmission electron microscopy (TEM), X-ray photoelectron spectroscopy measurements (XPS), N_2 adsorption–desorption isotherms and Barrett–Joyner–Halenda pore size distribution, and Raman spectroscopic. Please refer to support information for specific information.

2.3. Density functional theory calculation

All the calculations were performed within the framework of density functional theory (DFT) using the plane wave set Vienna ab initio Simulation Package (VASP) code [23, 24]. The supercell of graphene sheet and CoS_2/CoPS nanoribbon compound containing 109 atoms was used with the lattice of the unit cell set at 12.30Å×14.91Å×20Å (Fig. S1). The ORR/OER mechanism and the computational details of free energy are given in supplementary information.

2.4. Electrochemical measurement

2.4.1. ORR and OER test

Electrocatalytic activities were probed using a rotating disc electrode (RDE) with a Pine AFMSRCE rotation speed controller on an electrochemical workstation (CHI 760E work station) in a three-electrode system in 0.1 M KOH electrolyte in N_2- and O_2- saturated environment by using an Ag/AgCl and a Pt wire as reference and counter electrodes, respectively. The loading of electrocatalyst was 0.255 $mg \cdot cm^{-2}$. Electrochemical activity was studied by LSV with sweeping rates of 10 mV s^{-1} at different rotating speeds. The potential (E) range was calibrated to E_{RHE}, $E_{RHE}=E_{Ag/AgCl(3M\ KCl)}+0.209\ V+0.059\ V\times pH$.

2.4.2. Preparation of working electrode

The working electrode was composed of the catalytic layer, the current collector and the gas diffusion layer. In the catalytic layer, the as-synthesized samples were used

as the catalyst, active carbon was used as the additive, and Na_2SO_4 was used as the pore-forming agent. Above raw materials with a weight ratio of 0.1: 0.03: 0.02 g were milled with 0.3 mL polytetrafluoroethylene (PTFE, 60 wt.%) and ethanol solvent to produce a uniform paste. The uniform paste as the catalytic layer was laminated on one side of nickel foam by the roller press. The gas diffusion layer was composed of 0.3 g active carbon, 0.04 g Na_2SO_4, and 0.8 mL PTFE, it was laminated on other side of nickel foam by the roller press. Then above electrode was boiled for 10 min to form a gas-permeable/water-tight channels by remove Na_2SO_4 and to promote the curing of polytetrafluoroethylene. The thickness of working electrode (13 $mg \cdot cm^{-2}$ catalyst loading) was 0.7 mm.

2.4.3. Assembly of zinc–air battery

As-prepared working electrode and zinc plate were used as cathode and anode, respectively. The distance and active surface area of cathode and anode were 1.0 cm and 1.0 cm^2, respectively. The electrolyte was 6.0 M KOH.

2.4.4. Assembly of flexible zinc–air battery

As-prepared working electrode and zinc plate were also used as cathode and anode, respectively. The electrolyte was KOH/polyvinyl alcohol (PVA) gel and was prepared as follows: 3 g of PVA was first dissolved into 20 mL water under 85 °C, then 10 mL KOH (6 M) aqueous solution was added in above PVA solution for 1 hour under vigorous stirring. The mixture was placed at room temperature for 48 h to obtain the

solidified KOH/PVA gel. The gel was pressed on the as-prepared air–oxygen diffusion electrode, and metal zinc foil was pasted on the other side. After further solidification for 1 h, the flexible battery was packaged with a total thickness of 1.8 mm. The charge-discharge tests of all batteries were measured by a battery analyzer (A602-3008-3H2F-H) at different current densities.

3. Results and discussion

A schematic of the fabrication of the CoPS@SPNC is illustrated in Fig. 1a. Porous ZIF-67 crystals (Fig. S2a) with the particle size of 500 nm (Fig. S2b), the pore-size distribution range of 1.8–58.3 nm and the high level of microporosity (Fig. S2c) were fabricated through a typical room-temperature route [25]. After subsequent pyrolysis in N_2 atmosphere, the cobalt ions (II) were reduced into Co NPs and the ligand 2-methylimidazole was decomposed into mesopore graphite-type carbon with pyrrolic N, pyridine N, and quaternary N to generate Co@NC (Fig. S3 and Table S1). The optimal pyrolysis temperature of Co@NC is 600 °C because Co@NC-600 possesses the good crystalline property as supported by XRD (Fig. S3a) and Raman (Fig. S3e) results and the regular polyhedral morphology evidenced by SEM (Fig. S3j-l).

The as□prepared Co@NC-600 was simultaneously used for sulfidation and phosphidation with sulfur powder and $NaHPO_2$ powder under N_2 atmosphere at 300 °C, obtaining the CoPS@SPNC-600 sample. As shown in Fig. 1b, the XRD characteristic diffraction peaks of CoPS@SPNC-600 can be indexed to the coexistence of the cobalt phosphosulfide (CoPS) phase (PDF#27-0139) and the graphite-type carbon phase

(PDF#41−1487). The Raman spectrum of CoPS@SPNC-600 in Fig. 1c shows two intense bands at approximately 1378 and 1570 cm^{-1}, which correspond to D and G bands of the carbon matrix, respectively [26]. The graphitization of the carbon matrix in CoPS@SPNC-600 decreased compared with that in Co@NC-600 (Fig. S3e and Table S1), indicating the generation of more defects caused by S and P doping in the carbon matrix, as evidenced by the increased peak intensity ratio of I_D/I_G [27]. The existence and chemical valences of Co, C, N, S, and P with atomic values of 6.68, 49.84, 14.31, 19.97, and 9.19 at %, respectively, are further confirmed by XPS tests (Fig. S4 and Table S2).

Fig. 1d shows that the CoPS@SPNC-600 sample possesses H1 hysteresis loop and a type-IV isotherm, indicating a mesoporous feature [28, 29]. The pore size distribution in Fig. 1e displays that the CoPS@SPNC-600 sample has a pore size range of 1.7–53.5 nm. Compared with those in ZIF-67 (Fig. S2c), the decrease in the surface area and the increase in the pore size of CoPS@SPNC-600 sample suggest the transformation of microporous to mesoporous structure. The hierarchical pore structure is expected to create additional accessible catalytically active sites and provide multiple pathways for ion transfer [30].

The SEM image of CoPS@SPNC-600 reveals that the regular polyhedral structure was retained after the pyrolysis, vulcanization, and phosphating treatments (Fig. 1f). Compared with that in ZIF-67 (Fig. S2b), CoPS@SPNC-600 has a plane surface that is partially etched, leading to the emergence of concave morphology with rough and shrinking surfaces. Fig. 1g shows the TEM image of CoPS@SPNC-600, showing that

the CoPS NPs with a size range of 3 to 10 nm are well embedded in the porous carbon matrix [28]. The high-magnification TEM (HRTEM) image (Fig. 1h) displays NPs with clear regular lattice fringes of 0.271, 0.242, and 0.163 nm, corresponding to the (200), (210), and (311) planes of CoPS crystal, respectively. These results agree well with the XRD analysis (Fig. 1b). The EDS mapping (Fig. 1i) show that Co, C, N, S, and P are homogenously distributed throughout the hexagonal structure. Moreover, the coexistence of pyridine- N (398.7 eV), pyrrolic- N (400.3 eV), and quaternary- N (401.4 eV) is evidenced by the N 1s spectra (Fig. S4g). The N species would lead to different chemical/electronic environments for neighboring carbon atoms, thereby improving the electrocatalytic activities [31].

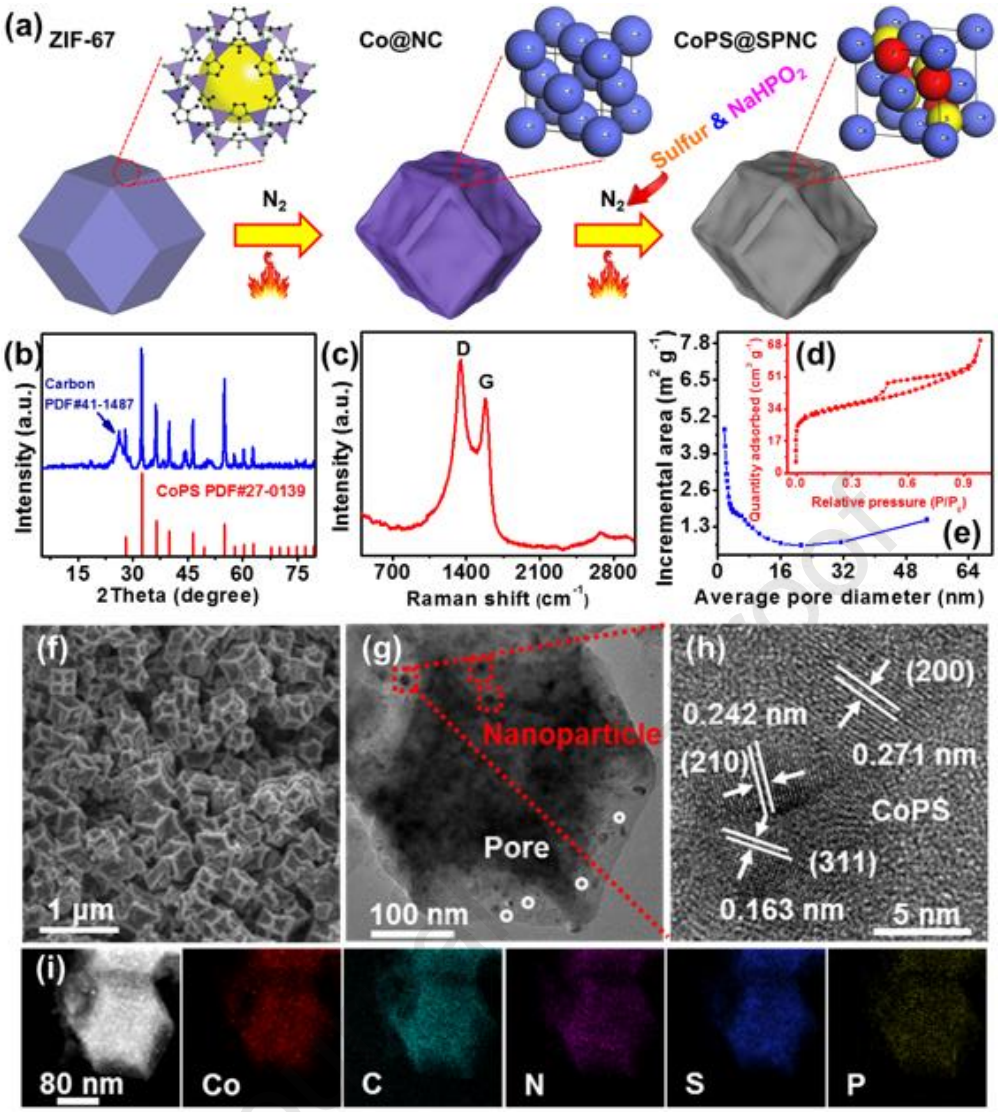

Fig. 1 (a) Scheme of the fabrication of electrocatalyst CoPS@SPNC-600. (b) XRD patterns, (c) Raman spectrum, (d) N_2 adsorption–desorption isotherms and (e) Barrett–Joyner–Halenda pore-size distribution, (f) SEM image, (g) TEM image, (h) HRTEM image, and (i) EDS elemental mapping images of CoPS@SPNC-600.

The free energy and overpotential (η) for each elementary reaction of all the possible sites on CoPS@SPNC were investigated by DFT calculations to check the rationality of our design, and CoS_2@SNC (Fig. S5) as the reference sample to highlight the role of P doping (Fig. 2a and b). For ORR, all elementary steps are downhill for

CoPS@SPNC and CoS_2@SNC, and the rate determining step is the third step, in which OH* was formed by adsorbing H on *O. The determining step occurs more preferably on CoPS@SPNC due to the relatively low reaction free energy of the third step (ΔG_3), suggesting that introducing P reduces the overpotential (with a reduction of 0.396 eV) of ORR for enhanced catalytic activity, consistent with the experimental results. The same conclusion can be drawn from the reaction-free energy diagram of the OER reaction steps (with an overpotential reduction of 0.253 eV), and the rate determining step is the sub-reaction, in which O* was transformed into OOH*.

According to the previous report, the overpotentials of ORR and OER are highly related to the adsorption of OH* [32], while the interaction between metal catalysts and intermediates is mainly through σ-bonds and π-bonds [33, 34]. The projected density of state (PDOS) analyses of the 3d orbital of Co site and the 2p orbital of O atom of OH* on CoS_2@SNC and CoPS@SPNC were performed (Fig. 2c and d). The PDOS diagrams displayed that the Fermi level (E_f) of Co (3d) and O (2p) in CoPS@SPNC falls on a peak near the pseudogap, while the E_f of Co (3d) and O (2p) in CoS_2@SNC falls in the pseudogap region. This finding illustrates the stronger interaction between Co site and OH* in CoS_2@SNC than that in CoPS@SPNC [35], which would lead to higher energy barrier in the following desorption process as well as higher reaction overpotential. Moreover, the d-band center of CoPS@SPNC (-2.14 eV) was more than that of CoS_2@SNC (-2.37 eV), facilitating the adsorption of reaction radicals [36]. It proves that CoPS@SPNC has better electrocatalytic performance than CoS_2@SNC.

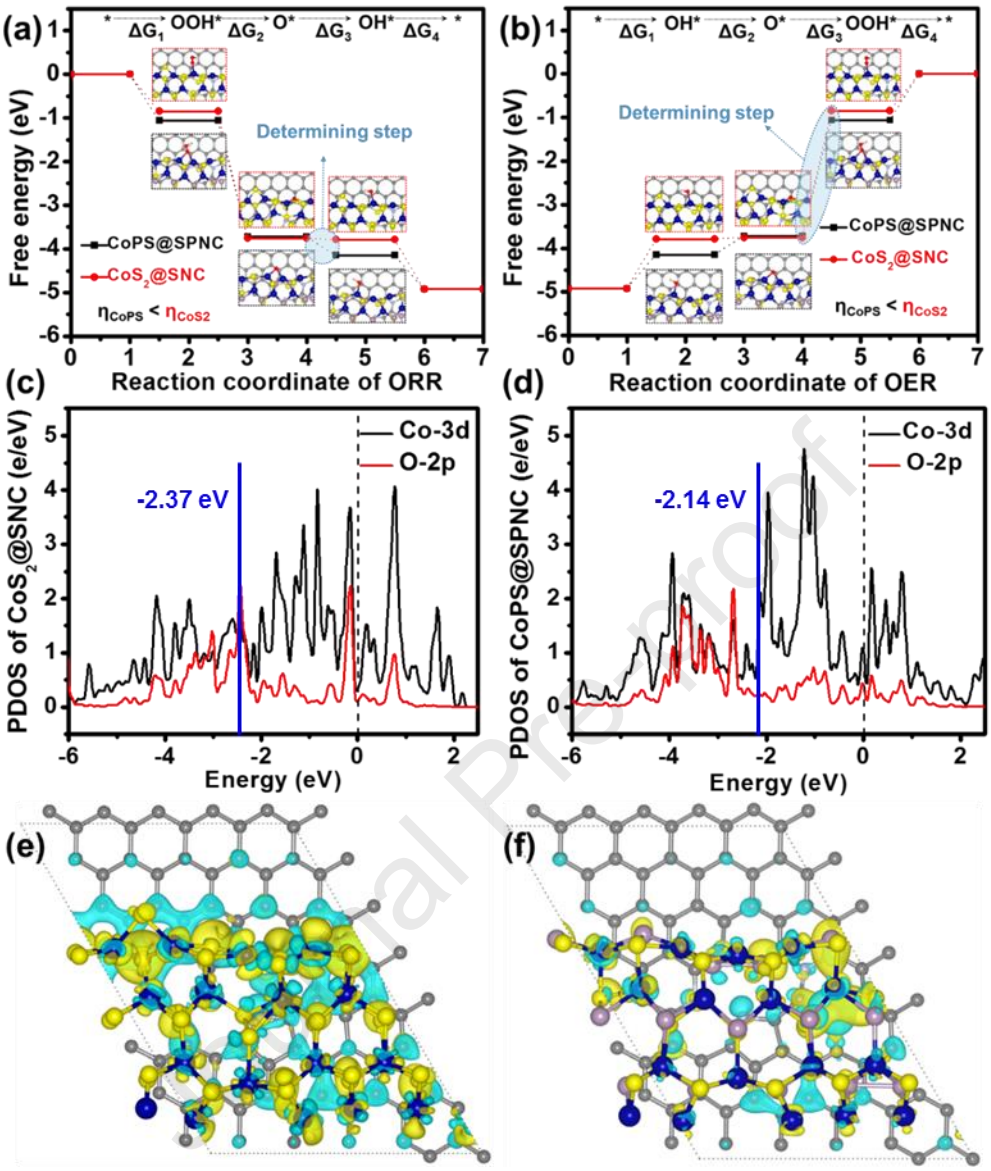

Fig. 2 Diagrams of ORR (a) and OER (b) substeps on Co site of CoS_2@SNC (red line) and CoPS@SPNC (black line). PDOS diagram of adsorbed on CoS_2@SNC (c) and CoPS@SPNC (d), the black and red line denote the 3d orbital of Co atom and the 2p orbital of O atom, respectively. Blue vertical line indicates the d-band center position. Top view of charge density difference distribution of (e) CoS_2 combined with SNC and (f) CoPS combined with SPNC. The C, N, S, P, and Co elements are represented by gray, light blue, yellow, purple, and dark blue. The yellow and blue isosurfaces with

isovalues of 0.00025 a_0^{-3} represent increased and decreased charge density respectively, where a_0 is the Bohr radius.

The charge density difference determined by subtracting the charge density of CoS_2/CoPS and the graphene substrate from the charge density of the combined compounds was evaluated to reveal the interaction between Co compounds and the carbon layer. Fig. 2e, f shows the charge transfer from the substrate to the compounds of Co, suggesting the synergistic effect between the carbon material and Co compounds. We can also conclude that the charge transfer tendency is receded in CoPS@SPNC, illustrating that CoPS exhibits more positive for the O_2 adsorption compared with CoS_2 when combined with the carbon substrate, which would account for the higher catalytic activity of CoPS@SPNC [37, 38].

RDE measurements in N_2- and O_2-saturated 0.1 M KOH were carried out to evaluate the OER and ORR performance of the as-prepared samples, respectively [39]. The benchmarks of Ir/C for OER and Pt/C for ORR are shown in Fig. S6. The LSV curves for the OER performance of the as-prepared catalysts are shown in Fig. 3a. CoPS@SPNC-600 displays the smallest overpotential of 314 mV at 10 mA cm^{-2}. Fig. 3b presents the overpotentials at 10 mA cm^{-2}, which were obtained from their corresponding LSV curves. The OER kinetics of the electrocatalysts was investigated by Tafel plot analysis (Fig. 3c). The smallest slope value of the Tafel plots for CoPS@SPNC-600 is 223.8 mV dec^{-1}.

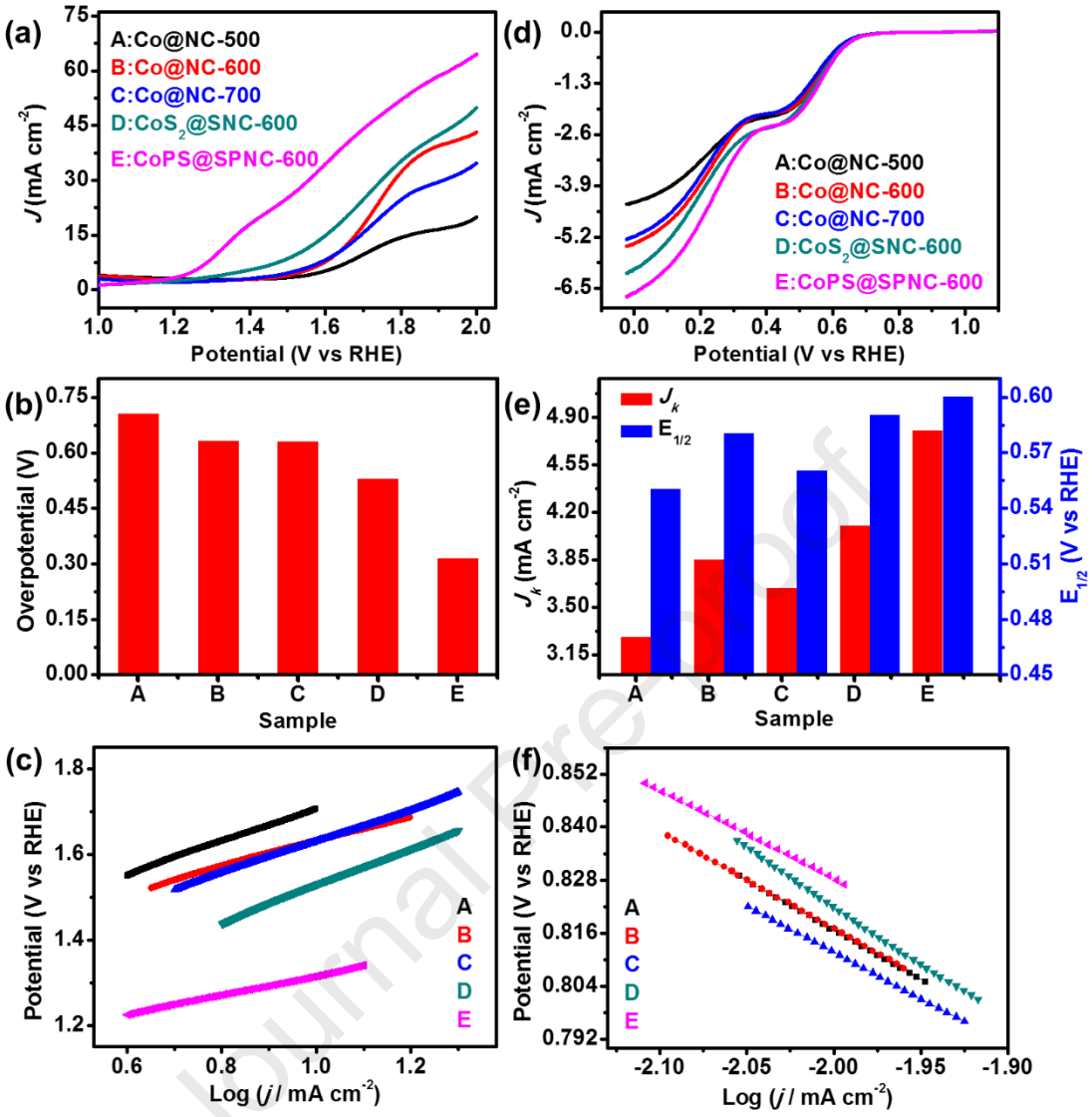

Fig. 3 (a) OER polarization curves, (b) overpotential required to reach J= 10 mA cm^{-2}, (c) OER Tafel plots, (d) ORR polarization curves, (e) comparison of J_k at 0.2 V and $E_{1/2}$, (f) ORR Tafel plots for Co@NC-500 (A), Co@NC-600 (B), Co@NC-700 (C), CoS_2@SNC-600 (D), and CoPS@SPNC-600 (E). J represents current density.

The ORR performance of the as-prepared catalysts was studied by LSV test (Fig. 3d). The half-wave ($E_{1/2}$) potentials and the kinetic current densities (J_k) at 0.2 V are shown in Fig. 3e. The $E_{1/2}$ values are 0.55, 0.58, 0.56, 0.59, and 0.60 V and the J_k values

at 0.2 V are 3.28, 3.85, 3.64, 4.10 and 4.80 mA cm^{-2} for Co@NC-500, Co@NC-600, Co@NC-700, CoS_2@SNC-600, and CoPS@SPNC-600, respectively. The comparative ORR kinetics of the electrocatalysts was further evaluated with the slope of Tafel plots in Fig. 3f. CoPS@SPNC-600 exhibits the smallest Tafel slope of 199.8 mV dec^{-1}. These results demonstrate that P doping can further improve the ORR activity and kinetics of CoPS@SPNC-600 compared with CoS_2@SNC-600. The excellent OER/ORR kinetics and the low overpotential of CoPS@SPNC-600 outperform most of the reported catalysts (Table S3), which may be attributed to the improvement of the mass/charge transfer caused by the synergistic effect between CoPS NPs and the defect-rich carbon.

For proof-of-application, we assembled the as-synthesized electrocatalysts into air cathodes for electrochemical experiments using the ZAB mold (Fig. S7a). Compared with the samples of Co@CN-500 and Co@CN-700, Co@CN-600 displayed the highest discharge voltage platforms with the increase in current density (Fig. S7b), indicating that this sample possesses the best discharge specific energy. As shown in Fig. 4a, after sulfidation, the obtained CoS_2@SNC-600 sample shows a discharge voltage platform of 1.322 V at 1 mA cm^{-2}. The CoPS@SPNC-600 sample exhibits an increased discharge voltage platform reaching to 1.415 V. Even at 20 mA cm^{-2}, the discharge voltage of CoPS@SPNC-600 can still reach 1.0 V. Fig. 4b shows the charge-discharge curves at 2 mA cm^{-2} of Co@NC-600, CoS_2@SNC-600, and CoPS@SPNC-600. Compared with that of Co@NC-600 (0.58 V, Fig. S7c), the voltage gaps of the charge-discharge curves of CoS_2@SNC-600 and CoPS@SPNC-600 are decreased to 0.32 and 0.2 V, respectively. Moreover, the ZAB cell with CoPS@SPNC-600 delivered the highest

discharge voltage of 1.36 V. These results suggest that sulfidation and phosphating facilitate the reduction in the overpotential of the ZAB. The reduced overpotential is beneficial to the improvement of energy efficiency. In Fig. S7d, the stable discharge voltage of Co@CN-600 after 12 h indicates its good stability compared with Co@CN-500 and Co@CN-700. As shown in Fig. 4c, CoS_2@SNC-600 displays improved discharge voltage compared with Co@NC-600, indicating the improvement of discharge energy density. However, the increased charge voltage leads the reduction of energy efficiency. Compared with CoS_2@SNC-600, CoPS@SPNC-600 exhibits higher discharge voltage (0.91 V) and lower charge voltage (2.34 V) without obvious change for 12 h, indicating that CoPS@SPNC-600 possesses the best cycle stability and the lowest overpotential (Fig. 4c). Moreover, the polarization curve and corresponding power density of Co@NC-600, CoS_2@SNC-600, and CoPS@SPNC-600 are shown in Fig. S8. The CoPS@SPNC-600 electrocatalyst possesses higher current density of 20 mA cm^{-2} at 1.0 V and higher peak power density of 25.9 mW cm^{-2} at 0.518 V than those of Co@NC-600 and CoS_2@SNC-600 under the same condition.

For proof-of-flexibility, we assembled a flexible ZAB through in-situ solidification composed of the optimized CoPS@SPNC-600 as air electrode, Zn plate as anode, and alkaline gel electrolyte (KOH/polyvinyl alcohol) as electrolyte (Fig. 4d). A single flexible ZAB in the form of a bracelet was fabricated to light up a light bulb, suggesting the great potential of this sample for commercial applications (Fig. 4e and 4f). Moreover, a flexible ZAB cut from the bracelet was bent to varying degrees of 108° (Fig. 4g), 49° (Fig. 4h), and 15° (Fig. 4i) to further assess its flexibility.

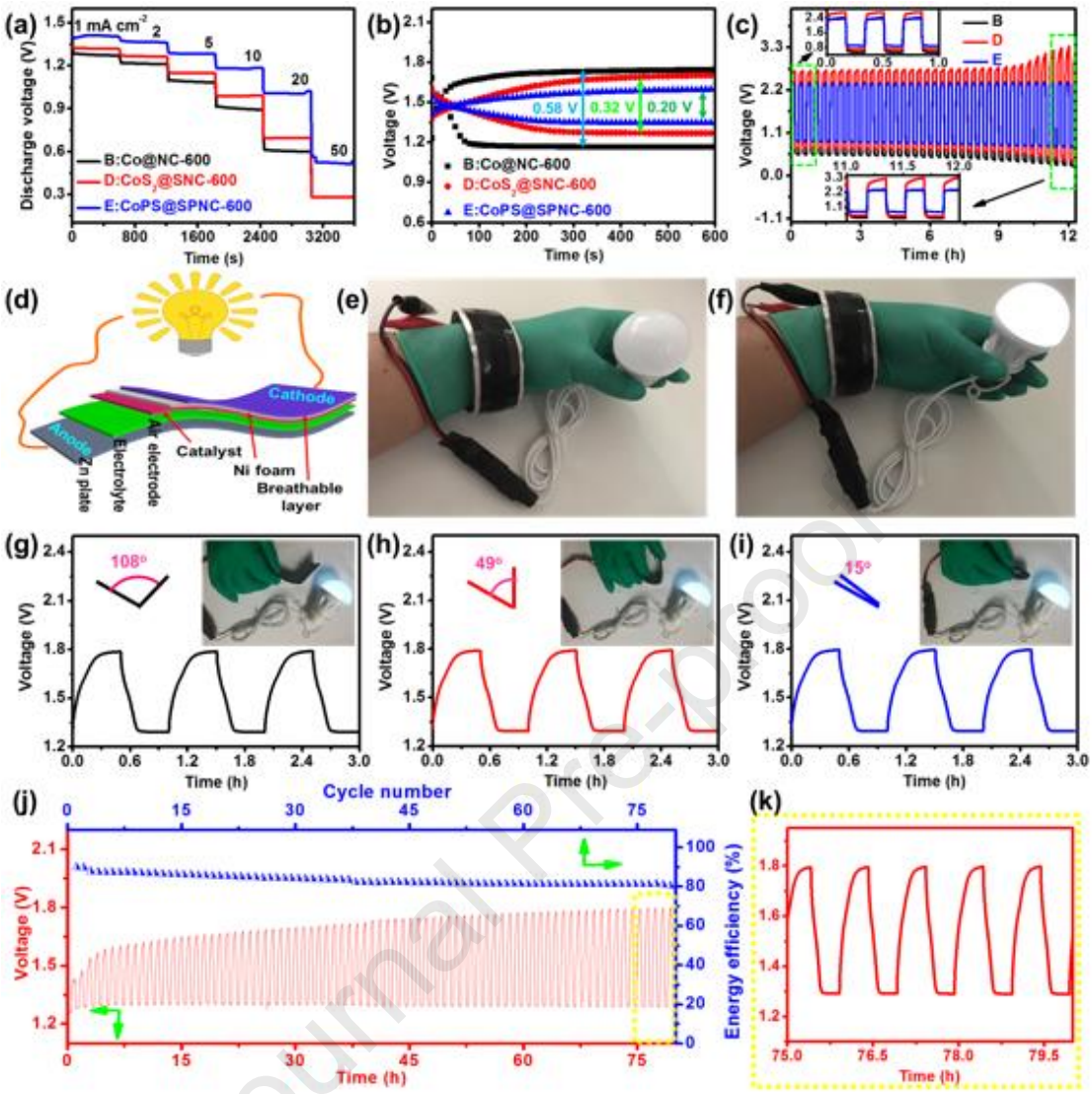

Fig. 4 (a) Discharge curves at different current densities. (b) First galvanostatic discharge–charge curves at 2 mA cm^{-2}. (c) Discharge–charge testing with each cycle consisting of 10 min discharge followed by 10 min charge at a current density of 20 mA cm^{-2}. (d) Schematic of the flexible ZAB. Display effect of Bracelet power supply device, (e) disconnecting the power, and (f) switching on the power. Bending property tests with galvanostatic charge-discharge; bending to (g) 108°, (h) 49°, and (i) 15°, respectively. (j) Galvanostatic charge–discharge curves and energy efficiency with each cycle consisting of 30 min charge followed by 30 min charge at a current density of 2 mA cm^{-2}. (k) Enlarged image of the charge–discharge curve in (j). B, D, and E represent

the cells with the Co@NC-600, CoS_2@SNC-600, and CoPS@SPNC-600.

The high flexibility of our device was revealed by the unchanged charge–discharge curves under all the tested conditions, indicating that our device is potentially useful for flexible and wearable electronics. As shown in Fig. 4j, the discharge–charge testing at 2 mA cm^{-2} exhibits a high stability without obvious loss of discharge performance and energy efficiency of more than 80% for 80 h. The enlarged picture of Fig. 4j shows relatively stable charge–discharge potentials of approximately 1.29 V in Fig. 4k because of the good structural stability (Fig. S9) of CoPS@SPNC-600 electrocatalysts. Notably, two voltage plateaus are observed in the charge–discharge curves. For charging, two plateaus represent oxidation of CoPS nanoparticles and the OER, respectively [40]. As for discharging, two plateaus represent the reduction of CoPS nanoparticles and the ORR, respectively [41]. Hence, CoPS@SPNC acts as both bifunctional oxygen electrocatalyst and electrochemical redox active species [42-44]. Compared with the reports in Table S4, our flexible device exhibits better performance, higher discharge voltage, and longer cycle stability, which are highly beneficial for next-generation flexible electronics with high energy density batteries.

4. Conclusions

In summary, we designed and synthesized CoPS@SPNC as bifunctional oxygen catalysts through carbonization of ZIF-67 followed by simultaneous sulfidation and phosphating treatment. The experimental and theoretical results demonstrated the

heterogeneous synergy between CoPS NPs and the SPNC carbon matrix. The introduction of P atoms can efficiently tune the charge distribution of the catalyst and provide a lower reaction-free energy for ORR and OER. The CoPS@SPNC-600 displayed the highest kinetics in ORR (a low Tafel slope of 199.8 mV dec^{-1}) and OER (a low Tafel slope of 223.8 mV dec^{-1}), stable discharge voltage of 1.36 V, and low overpotential of 0.20 V at 2 mA cm^{-2} in ZAB. Furthermore, the flexible ZAB with electrocatalyst CoPS@SPNC demonstrated a low overpotential of 0.49 V, an energy efficiency of >80%, and a discharge voltage of 1.29 V for 80 h at 2 mA cm^{-2}. This study highlights a novel strategy to create defect engineered metal sulfides/carbon hybrid from zeolitic imidazolate framework with excellent electrocatalytic performance for metal-air batteries.

Reference

[1] X. Xu, J. Mi, M. Fan, K. Yang, H. Wang, J. Liu, H. Yan, Study on the performance evaluation and echelon utilization of retired $LiFePO_4$ power battery for smart grid. J. Clean. Prod. 213 (2019) 1080-1086.

[2] M.C. Argyrou, P. Christodoulides, S.A. Kalogirou, Energy storage for electricity generation and related processes: Technologies appraisal and grid scale applications. Renew. Sust. Energy Rev. 94 (2018) 804-821.

[3] W. Zuo, R. Li, C. Zhou, Y. Li, J. Xia, J. Liu, Battery-supercapacitor hybrid devices: recent progress and future prospects. Adv. Sci. 4 (2017) 1600539.

[4] Y. Li, J. Fu, C. Zhong, T. Wu, Z. Chen, W. Hu, K. Amine, J. Lu, Recent advances in flexible zinc-based rechargeable batteries. Adv. Energy Mater. 9 (2019) 1802605.

[5] B. Liu, J.-G. Zhang, W. Xu, Advancing lithium metal batteries. Joule 2 (2018) 833-845.

[6] J. Qian, X. Guo, T. Wang, P. Liu, H. Zhang, D. Gao, Bifunctional porous Co-doped NiO nanoflowers electrocatalysts for rechargeable zinc-air batteries. Appl. Catal. B: Environ. 250 (2019) 71-77.

[7] Y. Qian, T. An, E. Sarnello, Z. Liu, T. Li, D. Zhao, Janus electrocatalysts containing MOF-derived carbon networks and NiFe-LDH nanoplates for rechargeable zinc–air batteries. ACS Appl. Energy Mater. 2 (2019) 1784-1792.

[8] Q. Hu, G. Li, G. Li, X. Liu, B. Zhu, X. Chai, Q. Zhang, J. Liu, C. He, Trifunctional electrocatalysis on dual-doped graphene nanorings-integrated boxes for efficient water splitting and Zn-air batteries. Adv. Energy Mater. 9 (2019) 1803867.

[9] T. Zhou, W. Xu, N. Zhang, Z. Du, C. Zhong, W. Yan, H. Ju, W. Chu, H. Jiang, C.

Wu, Y. Xie, Ultrathin cobalt oxide layers as electrocatalysts for high-performance flexible Zn-air batteries. Adv. Mater. 31 (2019) e1807468.

[10] X. Mao, C. Ling, C. Tang, C. Yan, Z. Zhu, A. Du, Predicting a new class of metal-organic frameworks as efficient catalyst for bi-functional oxygen evolution/reduction reactions. J. Catal. 367 (2018) 206-211.

[11] J. Sanetuntikul, S. Hyun, P. Ganesan, S. Shanmugam, Cobalt and nitrogen co-doped hierarchically porous carbon nanostructure: a bifunctional electrocatalyst for oxygen reduction and evolution reactions. J. Mater. Chem. A 6 (2018) 24078-24085.

[12] K. Mamtani, D. Jain, D. Dogu, V. Gustin, S. Gunduz, A.C. Co, U.S. Ozkan, Insights into oxygen reduction reaction (ORR) and oxygen evolution reaction (OER) active sites for nitrogen-doped carbon nanostructures (CNx) in acidic media. Appl. Catal. B: Environ. 220 (2018) 88-97.

[13] Y. Li, C. Zhong, J. Liu, X. Zeng, S. Qu, X. Han, Y. Deng, W. Hu, J. Lu, Atomically thin mesoporous Co_3O_4 layers strongly coupled with N□rGO nanosheets as high‐performance bifunctional catalysts for 1D knittable zinc–air batteries. Adv. Mater. 30 (2018) 1703657.

[14] J. Zhang, Z. Zhao, Z. Xia, L. Dai, A metal-free bifunctional electrocatalyst for oxygen reduction and oxygen evolution reactions. Nat. Nanotechnol. 10 (2015) 444-452.

[15] R. Ma, G. Lin, Y. Zhou, Q. Liu, T. Zhang, G. Shan, M. Yang, J. Wang, A review of oxygen reduction mechanisms for metal-free carbon-based electrocatalysts. npj Comput. Mater. 5 (2019) 78.

[16] Z. Zhang, Y.-P. Deng, Z. Xing, D. Luo, S. Sy, Z.P. Cano, G. Liu, Y. Jiang, Z. Chen, "Ship in a bottle" design of highly efficient bifunctional electrocatalysts for long-lasting rechargeable Zn-air batteries. ACS Nano 13 (2019) 7062-7072.

[17] L. Guo, J. Deng, G. Wang, Y. Hao, K. Bi, X. Wang, Y. Yang, N, P□doped CoS_2 embedded in TiO_2 nanoporous films for Zn–air batteries. Adv. Funct. Mater. 28 (2018) 1804540.

[18] Q. Shao, J. Liu, Q. Wu, Q. Li, H.-g. Wang, Y. Li, Q. Duan, In situ coupling strategy for anchoring monodisperse Co_9S_8 nanoparticles on S and N dual-doped graphene as a bifunctional electrocatalyst for rechargeable Zn–air battery. Nano-Micro Lett. 11 (2019) 4.

[19] S. Yang, L. Zhi, K. Tang, X. Feng, J. Maier, K. Müllen, Efficient synthesis of heteroatom (N or S)-doped graphene based on ultrathin graphene oxide-porous silica sheets for oxygen reduction reactions. Adv. Funct. Mater. 22 (2012) 3634-3640.

[20] Y. Li, J. Wang, X. Li, D. Geng, M.N. Banis, R. Li, X. Sun, Nitrogen-doped graphene nanosheets as cathode materials with excellent electrocatalytic activity for high capacity lithium-oxygen batteries. Electrochem. Commun. 18 (2012) 12-15.

[21] M. Prabu, P. Ramakrishnan, S. Shanmugam, $CoMn_2O_4$ nanoparticles anchored on nitrogen-doped graphene nanosheets as bifunctional electrocatalyst for rechargeable zinc–air battery. Electrochem. Commun. 41 (2014) 59-63.

[22] Y. Gao, Z. Xiao, D. Kong, R. Iqbal, Q.-H. Yang, L. Zhi, N, P co-doped hollow carbon nanofiber membranes with superior mass transfer property for trifunctional metal-free electrocatalysis. Nano Energy 64 (2019) 103879.

[23] G. Kresse, J. Furthmüller, Efficient iterative schemes for ab initio total-energy calculations using a plane-wave basis set. Phys. Rev. B 54 (1996) 11169-11186.

[24] G. Kresse, J. Furthmüller, Efficiency of ab-initio total energy calculations for metals and semiconductors using a plane-wave basis set. Comput. Mater. Sci. 6 (1996) 15-50.

[25] P. Deng, J. Yang, S. Li, T.-E. Fan, H.-H. Wu, Y. Mou, H. Huang, Q. Zhang, D.-L. Peng, B. Qu, High initial reversible capacity and long life of ternary SnO_2-Co-carbon nanocomposite anodes for lithium-ion batteries. Nano-Micro Lett. 11 (2019) 18.

[26] S. Liu, K.H. Kim, J.M. Yun, A. Kundu, K.V. Sankar, U.M. Patil, C. Ray, S.C. Jun, 3D yolk–shell $NiGa_2S_4$ microspheres confined with nanosheets for high performance supercapacitors. J. Mater. Chem. A 5 (2017) 6292-6298.

[27] L.G. Bulusheva, A.V. Okotrub, I.A. Kinloch, I.P. Asanov, A.G. Kurenya, A.G. Kudashov, X. Chen, H. Song, Effect of nitrogen doping on Raman spectra of multi-walled carbon nanotubes. Phys. Status Solidi B 245 (2008) 1971-1974.

[28] X. Zhang, X. Xu, W. He, G. Yang, J. Shen, J. Liu, Q. Liu, $LiFePO_4$/$NaFe_3V_9O_{19}$/porous glass nanocomposite cathodes for Li^+/Na^+ mixed-ion batteries. J. Mater. Chem. A 3 (2015) 22247-22257.

[29] X. Xu, Z. Hao, H. Wang, C. Hu, J. Liu, Y. Jin, In-situ preparation of mesoporous carbon contained graphite-zinc quantum dots for enhancing the electrochemical performance of $LiFePO_4$. Ionics 25 (2018) 89-98.

[30] Z. Wang, W. Xu, X. Chen, Y. Peng, Y. Song, C. Lv, H. Liu, J. Sun, D. Yuan, X. Li, X. Guo, D. Yang, L. Zhang, Defect‐rich nitrogen doped Co_3O_4/C porous nanocubes

enable high‐efficiency bifunctional oxygen electrocatalysis. Adv. Funct. Mater. 29 (2019) 1902875.

[31] X. Xu, Z. Hao, H. Wang, Y. Xie, J. Liu, H. Yan, A facile synthetic route of nitrogen-doped graphite derived from chitosan for modifying $LiFePO_4$ cathode. J. Mater. Sci.: Mater. Electron. 29 (2018) 16630-16638.

[32] M. Li, L. Zhang, Q. Xu, J. Niu, Z. Xia, N-doped graphene as catalysts for oxygen reduction and oxygen evolution reactions: theoretical considerations. J. Catal. 314 (2014) 66-72.

[33] F. Lima, J. Zhang, M. Shao, K. Sasaki, M. Vukmirovic, E. Ticianelli, R. Adzic, Catalytic activity−d-band center correlation for the O_2 reduction reaction on platinum in alkaline solutions. J. Phys. Chem. C 111 (2007) 404-410.

[34] I.C. Man, H.Y. Su, F. Calle□Vallejo, H.A. Hansen, J.I. Martínez, N.G. Inoglu, J. Kitchin, T.F. Jaramillo, J.K. Nørskov, J. Rossmeisl, Universality in oxygen evolution electrocatalysis on oxide surfaces. ChemCatChem 3 (2011) 1159-1165.

[35] P. Ravindran, B. Johansson, O. Eriksson, Electronic structure, chemical bonding, phase stability, and ground-state properties of $YNi_{2-x}(Co/Cu)_xB_2C$. Phys. Rev. B 58 (1998) 3381.

[36] Z.P. Wang, Z.P. Lin, J. Deng, S.J. Shen, F.Q. Meng, J.T. Zhang, Q.H. Zhang, W.W. Zhong, L. Gu, Elevating the d-band center of six-coordinated octahedrons in Co_9S_8 through Fe-incorporated topochemical deintercalation. Adv. Energy Mater. 11 (2021) 2003023.

[37] A. Shen, W. Xia, L. Zhang, S. Dou, Z. Xia, S. Wang, Charge transfer induced

activity of graphene for oxygen reduction. Nanotechnol. 27 (2016) 185402.

[38] L. Zhang, Z. Xia, Mechanisms of oxygen reduction reaction on nitrogen-doped graphene for fuel cells. J. Phys. Chem. C 115 (2011) 11170-11176.

[39] R. Ma, G. Lin, Q. Ju, W. Tang, G. Chen, Z. Chen, Q. Liu, M. Yang, Y. Lu, J. Wang, Edge-sited Fe-N_4 atomic species improve oxygen reduction activity via boosting O_2 dissociation. Appl. Catal. B: Environ. 265 (2020) 118593.

[40] P. Tan, B. Chen, H. Xu, W. Cai, W. He, M. Ni, In-situ growth of Co_3O_4 nanowire-assembled clusters on nickel foam for aqueous rechargeable Zn-Co_3O_4 and Zn-air batteries. Appl. Catal. B: Environ. 241 (2019) 104-112.

[41] P. Tan, B. Chen, H. Xu, W. Cai, W. He, M. Liu, Z. Shao, M. Ni, Co_3O_4 nanosheets as active material for hybrid Zn batteries. Small 14 (2018) e1800225.

[42] Y. Ma, W. Shang, W. Yu, X. Chen, W. Xia, C. Wang, P. Tan, Synthesis of ultrasmall $NiCo_2O_4$ nanoparticle-decorated N-doped graphene nanosheets as an effective catalyst for Zn–air batteries. Energy Fuel. 35 (2021) 14188-14196.

[43] P. Tan, B. Chen, H. Xu, W. Cai, W. He, M. Ni, Porous Co_3O_4 nanoplates as the active material for rechargeable Zn-air batteries with high energy efficiency and cycling stability. Energy 166 (2019) 1241-1248.

[44] W.X. Shang, W.T. Yu, P. Tan, B. Chen, Z. Wu, H.R. Xu, M. Ni, Achieving high energy density and efficiency through integration: progress in hybrid zinc batteries. J. Mater. Chem. A 7 (2019) 15564-15574.

Declaration of interests

☒The authors declare that they have no known competing financial interests or personal relationships that could have appeared to influence the work reported in this paper.

☐The authors declare the following financial interests/personal relationships which may be considered as potential competing interests: